Probing the Mechanisms of Global Brain Reconfiguration after Local Manipulations

Giovanni Rabuffo[†1*], Houefa-Armelle Lokossou[†1,2], Zengmin Li[†3], Abolfazl Ziaee-Mehr[1], Meysam Hashemi[1], Pascale P Quilichini[1], Antoine Ghestem[1], Ouafae Arab[1], Monique Esclapez[1], Parul Verma[4], Ashish Raj[4], Alessandro Gozzi[5], Pierpaolo Sorrentino[1], Kai-Hsiang Chuang[3], Teodora-Adriana Perles-Barbacaru[2], Angèle Viola[2], Viktor K. Jirsa[1*] and Christophe Bernard[1*]

[1]Institut de Neurosciences des Systèms, Aix Marseille University, UMR 1106 INSERM, Marseille, France.
[2]Center for Magnetic Resonance in Biology and Medicine, Aix-Marseille University, UMR 7339 CNRS, Marseille, France.
[3]Queensland Brain Institute , The University of Queensland, Brisbane, Australia.
[4]University of California, UCSF, San Francisco, USA.
[5]Functional Neuroimaging Laboratory, Istituto Italiano di Tecnologia, Rovereto, Italy.

*Corresponding author(s). E-mail(s): giovanni.rabuffo@univ-amu.fr; viktor.jirsa@univ-amu.fr; christophe.bernard@univ-amu.fr;

Abstract

Various techniques, including optogenetics, chemogenetics, electrical stimulation, and lesions are used to probe brain function and dysfunction. However, the mechanistic consequences of such manipulations at the whole-brain scale remain poorly understood. This information is necessary for a proper interpretation of the functional consequences of local alterations. Combining mouse experimental datasets of focal interventions (thalamic lesion and chemogenetic silencing of cortical hubs), we demonstrate both local and global effects. Utilizing advanced whole-brain simulations of experimental data, we not only confirm the

[†]Co-first authors

distributed nature of local manipulations but also offer mechanistic insights into these processes. Our simulations predict that the reconfiguration of hemodynamic functional connectivity is tightly coupled with the modulation of neurophysiological activity. This includes alterations in firing rates and spectral characteristics across specific brain networks, leading to structured changes in functional connectivity patterns. Crucially, the brain subnetworks most profoundly impacted are contingent upon the precise site of local intervention. Thus, these subnetworks serve as distinctive fingerprints, enabling pinpoint localization of the altered brain region. This knowledge holds the potential to inform clinical decision-making and address focal brain pathologies by developing circuit-level interventions and customized neuromodulation therapies.

Keywords: Mouse fMRI, Resting-state, Thalamic lesion, Chemogenetic silencing, Brain models, Inference, Multiscale mechanisms

1 Introduction

Insights into brain function and dysfunction are usually obtained by interfering with neuronal activity and studying the brain's response to such perturbations. This allows for establishing cause-effect relationships and proposing mechanisms. For example, optogenetics or chemogenetics are used to control specific cell types in specific brain regions, in order to identify the role of these cells in a particular function or behavior [1, 2]. However, if causal links (e.g., exciting cell type X causes behavior Y) can be established, claiming that cell type X is responsible for, or controls, behavior Y is not as straightforward as it seems. The brain is a complex system characterized by a nested multi-level organization, and emergent system-level properties arise from intricate interactions among its constituents[3]. In such a system, it is difficult to identify which cell is responsible for what. In a simple behavioral task, many cell types scattered throughout the brain respond to a visual stimulus or during a motor command [4]. Conversely, the activity of a few neuronal units has the potential to reshape the system-level organization [5]. Similarly, direct stimulation or focal brain lesions produce both short-range (local, where the intervention takes place) and long-range (at distant brain sites) effects, a phenomenon known as focal diaschisis [6, 7]. Focal diaschisis has been found in humans and mice within intact brain regions not directly affected by a lesion [6, 8–12]. Focal lesions can also affect large-scale network organization, by changing functional connectivity [13], possibly by changing neuronal excitability or receptor density [14, 15]. In mice, selective silencing or activation of neuronal cells increased functional connectivity [16], a result replicated in non-human primates [17]. In contrast, focal inhibition of cortical hubs leads to reduced functional connectivity [18]. Since multiple local stimulation paradigms (e.g. deep brain stimulation and transcranial magnetic stimulation) have been developed to treat brain disorders in patients, it is important to determine and predict both local and global

effects. A better understanding of the consequences of local interventions may also help identify where to intervene to obtain an optimal therapeutic effect, as opposed to the present empirical approaches. To characterize the effects of local interventions at the whole brain scale, we analyzed two independent datasets consisting of functional magnetic resonance imaging (fMRI) acquired in mice cohorts pre- and post-silencing of specific brain sites. In the first dataset, thalamic brain regions were lesioned, whereas, in the second dataset, cortical functional hubs of the mouse were chemogenetically silenced. In order to shed light on the underlying mechanisms, we leverage whole brain models [19, 20] and simulation-based inference (SBI) [21–23], to virtualize the mouse brain and study the effects of focal silencing at the physiological and functional levels in silico.

2 Results

We analyzed two independent datasets (Fig.1.A, Suppl.Fig.1) to investigate the effects of inactivating a focal area of the brain on whole-brain dynamics. In a 'Lesion' dataset, we used an irreversible lesion of thalamic nuclei by excitotoxic neurodegeneration produced by local administration of N-methyl-D-aspartate (NMDA) injection (Th; 6 C57BL6 mice). In this group, Blood-oxygen-level-dependent (BOLD) acquisitions were performed in 'resting-state' fMRI (rs-fMRI) under light anesthesia before and 6 weeks after the lesion (Suppl.Fig.1, histology). In a 'DREADD' dataset, C57Bl/6J mice were recorded under light anesthesia, before and 30 minutes after clozapine-N-oxide (CNO) injection causing DREADD-mediated pan-neuronal inhibition of either the anterior cingulate area (ACA; 7 mice) or the retrosplenial cortex (RSC; 14 mice). A control group (CTRL; 8 mice) underwent the same experimental pipeline as the RSC group, but the mice were not expressing DREADD (Suppl.Fig.1, experimental figures). We first compared voxel-level Functional Connectivity (FC), defined as Pearson's correlation over all voxel pairs, before and after focal silencing (Fig.1.A). Figure 1.B shows, for each voxel (order of 1 mm^3) the mean of the FC matrix across one of the two axes, averaged across all pre-lesion (left) and pre-DREADD (right) mice. This measure is sometimes referred to as 'weighted degree centrality' [24] or 'global connectivity' [25] since the FC degree corresponds to the average correlation between a voxel and the rest of the network. For the sake of consistency with the forthcoming analyses, we will use the term 'mean Coordination' to refer to this measure (see also Fig.2.A and subsection 2.2). Upon visual inspection, these brain plots reveal that cortical voxels are well coordinated with the whole-system activity, while the mean Coordination gradually decreases in a gradient towards subcortical structures.These results were consistent across datasets, despite the different spatial and temporal resolutions (see Methods). In the DREADD groups, for which we have more mice with higher temporal resolution (2000 time points), the average pre-DREADD mouse data revealed a strong coordinated core (in yellow) along the cortical midline structures, with a peak in the deep cortical

layers and in the dentate gyrus. These regions roughly correspond to what was previously identified as the mouse default mode network (DMN; [26]). These results show that, as previously reported[25], mouse rsfMRI is organized in functional networks, with specific subsets of voxels that are highly coordinated to whole-brain network fluctuations.

2.1 Widespread decrease of functional connectivity after focal region silencing

To probe the impact of focal region silencing on brain-wide measure of functional connectivity, for each mouse, we evaluated the difference between the mean Coordination post- and pre-silencing (Delta Mean Coordination; DMC) to assess the whole brain consequences of focal manipulations. Analyses of Th-, ACA-, and RSC-manipulated mice, revealed that after lesion/silencing, the mean Coordination patterns (Fig.1.B) were disrupted, revealing a decreased mean Coordination (dark blue) beyond the local neighborhood of the target regions (Fig.1.C). The DMC observed in the CTRL group was much smaller than in the RSC (and ACA) group. To validate this finding, we compared the distributions of the DMC (i.e., the values of the voxels as displayed in Figure 1.C) in RSC versus CTRL and found them to be statistically different (Kolmogorov-Smirnov statistics $KS = 0.62$, $p < 0.001$). The DMC distribution exhibited a leftward shift for Th, ACA, and RSC groups but not for the CTRL, showing that after silencing, a general decrease of whole-brain FC occurs (Fig.1.D; mean values: $\mu_{th} = -0.0026, \mu_{ACA} = -0.0087, \mu_{RSC} = -0.0113, \mu_{CTRL} = 0.0007$). Nonetheless, in all groups, the mean Coordination increased in a subset of voxels (positive DMC values), indicating that FC also increased along some pathways after focal silencing. We also noticed that the DMC distribution of the RSC group is skewed to the left, unlike the CTRL group, which appears to be more symmetric (Fisher-Pearson skewness coefficient $g_{RSC} = -0.72, g_{CTRL} = 0.10$). The same trend was evident for ACA ($g_{ACA} = -0.38$). This indicates that a subset of voxels is more prominently affected by chemogenetic silencing than others. In contrast to RSC and ACA, the Th group showed, to a lesser extent, some skewness to the left ($g_{Th} = 0.14$). We then identified the voxels most prominently affected by the chemogenetic silencing of RSC, for which we have the control group (CTRL). For each voxel, we compared with a Mann-Whitney U test the difference in mean Coordination (global connectivity) values measured before and after chemogenetic silencing. In Figure 1.E, we plot the significance values for each voxel. Importantly, the significance mask exhibited high spatial structure, demonstrating a topography of the voxels that significantly decreased after the RSC silencing. To interpret this result, we grouped the voxels according to the Allen Atlas mouse brain parcellation [27] with $N = 148$ regions of interest (ROIs; see Table 1) and computed the percentage of voxels significantly affected by the silencing within each brain region. This percentage was compared against a benchmark by randomly shuffling the significance mask. In Figure 1.F, we show in blue the ROIs with an unexpectedly low number of significantly decreased voxels

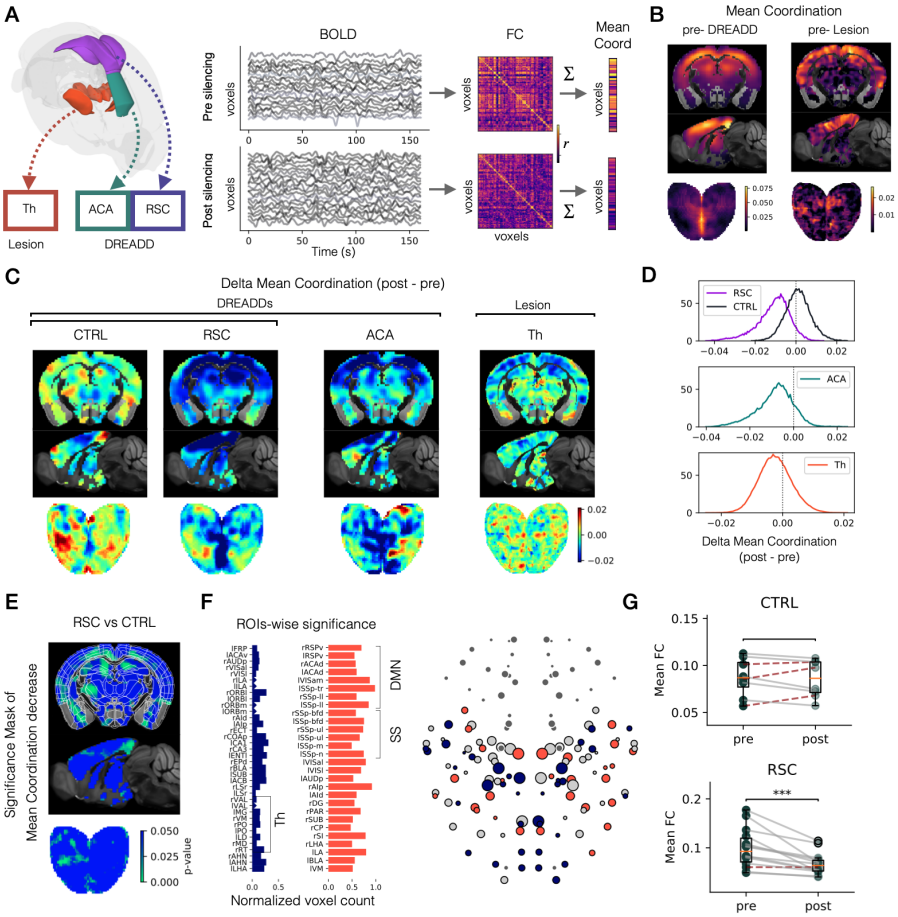

Fig. 1 Focal silencing induces functional connectivity reconfiguration: A) We analyzed two independent datasets where mice were recorded before and after silencing a brain region. Silencing was obtained by either lesion of a few Thalamic (Th) nuclei, or by chemogenetic (DREADD) inhibition of the anterior cingulate area (ACA) or the retrosplenial (RSC; dorsal and ventral) cortices. For pre- and post-silencing data we extracted the voxel-level FC and the mean Coordination (i.e., the FC degree), defined as the average correlation of the voxel with the rest of the voxels. B) Mean Coordination obtained by averaging across pre-lesion data and all pre-DREADD data. Note that the mean Coordination decreases along a dorsoventral axis and is higher in cortical regions. C) The Delta (post-pre) Mean Coordination (DMC) plotted for all the groups reveals that, after the focal silencing, a distributed decrease of mean Coordination is observed (dark blue) in all groups. The control group remains globally similar between post and pre (CTRL; sham of the RSC). D) The distribution of the DMC values in panel (C) is shifted to the left and skewed in all groups but not in the CTRL, which indicates an overall decrease in mean Coordination after focal silencing. (E) For the statistical significance of the mean Coordination decrease, we performed the Mann-Whitney U test in each voxel, comparing mice in the RSC group to mice in the CTRL group (green values indicate significance $p < 0.05$). F) Regions of interest (ROIs) with an unexpected percentage of decreased and increased voxels compared to null models. Regions showing an unexpected decrease (in blue) include most Thalamic nuclei, while those showing an unexpected increase (in red) include regions within the Default Mode Network (DMN) and the Somatosensory (SS) network, among others. G) RSC silencing resulted in decreased mean FC in 13 mice (continuous grey lines) and an increase in 1 mouse (dashed red lines). In the CTRL group, 5 mice decreased and 3 increased post-CNO injection. Only in the RSC group, the mean FC decrease was significant (Wilcoxon signed-rank test $p < 0.001$).

(i.e., ROIs that were expected to have more significant voxels according to the randomized masks), including a distributed network of regions and most thalamic nuclei. The ROIs with a higher-than-expected percentage of significantly decreased voxels (in red), include DMN and somatosensory (SS) ROIs, among other regions.

Finally, we show that a chemogenetic-induced decrease in correlation is also observable at the level of ROIs-reconstructed signals (see Appendix A). To this end, we first averaged the activities of all the voxels belonging to each region, which defined region-specific (order of $\sim 1-10mm^3$) BOLD time series. Adjacency (FC) matrices were computed for each subject before and after region silencing. Figure 1.G shows the average FC for each mouse of the RSC and CTRL groups, which significantly decreased only in the RSC group. Together, these results show that silencing specific brain regions results in widespread but structured reorganization of large-scale FC at rest. Because FC provides a static vision by averaging activity over the scanning time, we next performed a more detailed analysis focusing on brain dynamics at the timescale of the BOLD signal.

2.2 Changes in whole brain dynamics after focal region silencing

At rest, brain dynamics is characterized by the occurrence of intermittent bursts of activity [28–30]. During such bursts, many (sometimes very distant) brain regions display sudden co-fluctuations, giving rise to system-level correlations [31]. We thus hypothesized that the observed disruption of system-level correlations following focal region silencing (Fig.1) would be associated with a reduced capability of the network to generate widespread coordinated bursting. To test this hypothesis, we use an edge-wise perspective [28], whereby regions (or voxels) are regarded as network nodes, and the element-wise product of any two z-scored regional signals $Z_i(t)$ and $Z_j(t)$ define an edge co-fluctuation time series $E_{ij}(t) = Z_i(t) \cdot Z_j(t)$ (Fig.2.A). The edge co-activation matrix can be considered as a time-resolved FC at the timescale of the BOLD signal since the Pearson's correlation coefficient between node i and j is defined as the time average of their co-fluctuations i.e., $r = \langle E_{ij}(t) \rangle_t$. In other words–as sketched in Figure 2.A–the FC matrix (in purple) corresponds to the time average of the co-activation matrices (in green). Averaging the co-activation signals across all network edges defines the network dynamic profile $NDP(t) = \langle E_{ij}(t) \rangle_{ij}$. Such profile (corresponding to the square of the global signal $GS(t) = \langle Z_i(t) \rangle_i$; see Methods) follows a fat-tailed distribution (Fig.2.B). Rare high-amplitude events in the NDP correspond to strong simultaneous co-fluctuations of a large set of edges.

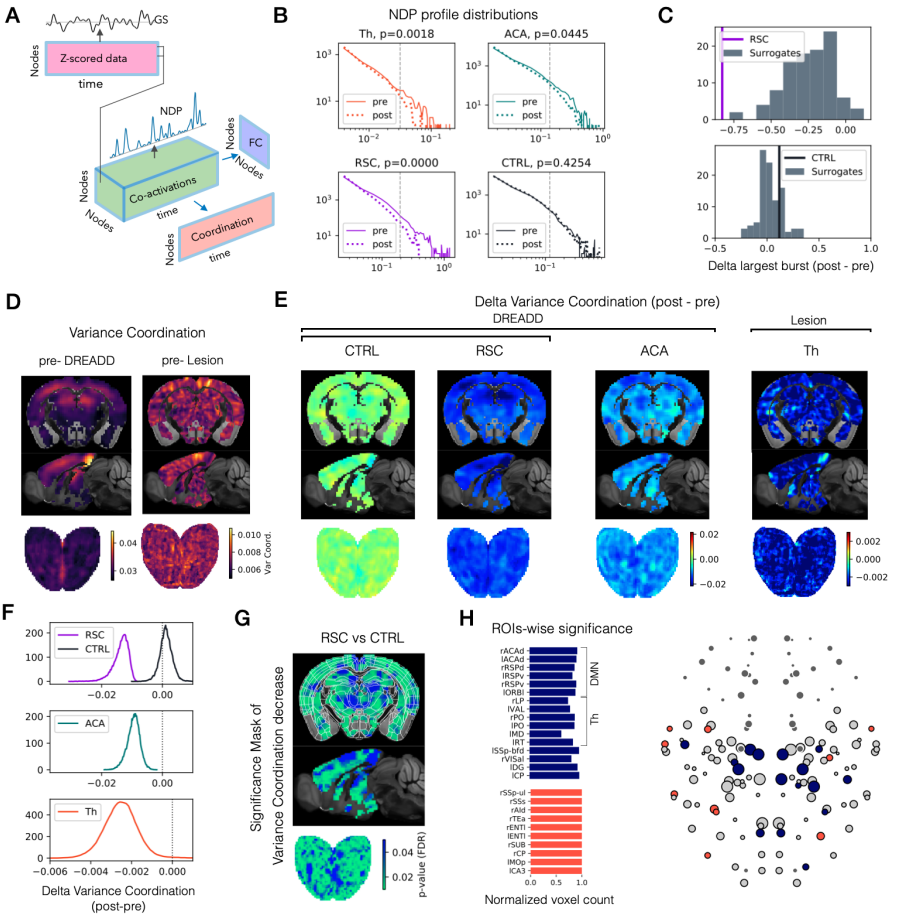

Fig. 2 Dynamic origin of FC decrease after focal lesion: A) Illustration of the analytic link between z-scored brain signals, edge co-activations, dynamic network profile (DNP), FC, and the Coordination measure. Each arrow represents the correlation along the parallel axis. Here the nodes can correspond to voxels or ROIs. B) The pre-silencing NDP distribution (continuous lines) is fat-tailed, indicating the presence of large-scale bursts of co-activations in the data. After focal silencing (dashed lines) the NDP decreases, showing an impaired capability of bursting. This effect was significant in RSC, ACA, and Th groups, but not in the CTRL group (Kolmogorov–Smirnov test performed for values above the dashed vertical lines; see p-values in the figure). C) The difference in the size of the largest burst between post and pre-silencing i.e., the largest value of the NDP is shown in purple and black for the RSC and CTRL groups, respectively. Surrogates (grey distributions) cannot explain the largest NDP bursts in the RSC. D-H) As panels B-F in Figure 1, for the Coordination variance instead of the mean Coordination. These results reveal even more widespread effects of focal silencing than those observed in Figure 1, which were based on static FC.

We compared the NDP profiles (pooled together for all mice within each group) before and after the regional silencing (Fig.2.B). The NDP distribution of the Th, ACA, and RSC groups exhibited a faster decrease in post-silencing recordings than in pre-silencing ones (the p-values of the Kolmogorov-Smirnov statistic in Fig.2 are evaluated considering bins above the dashed gray line). This result aligns with our hypothesis that the observed FC decrease caused by focal silencing is associated with a decrease in spontaneous network bursting. Importantly, this decrease does not occur in the CTRL group (Fig.2.B).

The decrease in large network bursts observed in the RSC may be a direct consequence of the decrease in FC identified above (Fig.1). Alternatively, it may reflect a genuine dynamical impairment. To disambiguate this dichotomy, we compared the NDP distribution to 100 surrogate datasets obtained from phase-randomization (cross-spectrum preserved) of the voxel signals (see Methods). This kind of surrogate data maintains the static correlation between voxel pairs (i.e., the static FC), so that each surrogate shows the same decrease of mean Coordination displayed in the panels in Figure 1. In Figure 2.C, we show that the maximum burst size observed in the RSC data (purple vertical line) is significantly lower than the maximum value expected from the surrogate NDPs (gray distribution). The same result does not hold for the CTRL group. We conclude that the decrease in static FC observed in our data does not fully explain the absence of large-scale bursts after the silencing of RSC. This observation suggests that focal silencing impairs spontaneous network bursting.

2.3 Altered local to global coordination dynamics

To investigate how the local activity of each voxel relates to the altered global bursting at the system level, for each voxel (network node i), we defined a metric of local-to-global Coordination, which describes the degree of participation of voxel i with the global signal fluctuations in a time-resolved way. Coordination is defined as the element-wise product $C_i(t) = Z_i(t) \cdot GS(t)$ of the voxel (standardized) activity $Z_i(t)$ and the global signal $GS(t)$. The Coordination corresponds to the average co-fluctuations of all the edges ij hinging on voxel i i.e., $C_i(t) = \langle E_{ij}(t) \rangle_j$ (as illustrated in Fig.2.A). For a given voxel, strong Coordination corresponds to moments when the voxel is co-fluctuating with the rest of the network, whereas weak Coordination corresponds to moments when the voxel is disjoint from the rest of the brain (or when the global signal is close to zero). In Figure 2.D-H, we show that the variance of the Coordination displays a precise, non-random topology that is reminiscent of the voxel-level differences described in Figure 1.B-E. The variance of the Coordination represents the ability of a region to dynamically fluctuate in and out of coordination with the rest of the network. Fluctuations are considerably reduced after the chemogenetic silencing of RSC, while they are not affected in the CTRL group (Fig.2.G-H). The analysis of the Coordination variance revealed stronger and even more widespread effects of focal silencing, as compared to the mean Coordination. For example, comparing Figure 1.D to Figure

2.F, one can observe that the distributions in the latter are further left to zero, indicating a net decrease in voxels dynamics. The voxel-wise significance test in Figure 2.G highlights widespread significant changes in Coordination variance that, differently from Figure 1.D, survive the FDR test. ROIs-level analysis revealed that fewer voxels than expected decreased in Coordination in several DMN and thalamic regions (Fig.2.H).

Collectively, these results demonstrate a clear reduction in static FC and dynamic network properties following either the chemogenetic inhibition of cortical hubs (RSC and ACA)[32], or the lesion of thalamic (Th) nuclei. Since previous works suggest the onset of fMRI over-connectivity after focal chemogenetic silencing in the mouse [16] and non-human primates [17], we focused on the DREADD RSC dataset and we used a computational approach to investigate the origin of this discrepancy.

2.4 Virtual Mouse Brain simulation

Although fMRI data provides a readout of whole brain dynamics, the underlying neuronal electrical signals remain hidden. Since DREADD silencing corresponds to greatly reduced neuronal excitability [1], the mechanisms underlying the observed results can only be interpreted in the light of the underlying neuronal activity. To this aim, we simulated realistic whole-brain activity using The Virtual Mouse Brain (TVMB) pipeline [19, 20] (see Methods). We focused on the RSC group and we built an in silico model of the pre-DREADD fMRI activity, that reproduced the average data features observed in the RSC mice before silencing. Simulated data (Fig.3.A) includes fast neuroelectric activity (e.g., average firing rate dynamics; 1000Hz sampling rate) as well as slow BOLD activity (0.5Hz sampling rate), which can be directly compared to empirical observations. The simulated activities depend on the choice of local and global model parameters. The main parameters for our simulations are the local node excitability η and the global coupling G. The latter measures the impact of structural connectivity on local dynamics: for $G = 0$ the regions are effectively decoupled while increasing G the regions are more driven by their mutual coupling. Brain heterogeneity was modeled by associating different excitability values to nodes belonging to different mouse resting-state networks identified according to a common classification (as in Suppl.Fig.2): Default Mode Network (DMN), Lateral Cortical Network (LCN), Visual Network (Vis), Basal-Frontal Network (BF), Hippocampal Formation (HPF), and Thalamus (TH). In total, our model has seven free parameters $(G, \eta_{DMN}, \eta_{Vis}, \eta_{LCN}, \eta_{BF}, \eta_{HPF}, \eta_{Th})$.

In order to simulate realistic empirical data, the identification of the sets of free parameters that most closely reproduce empirical pre-DREADD data in silico is required. To this aim, we used a simulation-based inference (SBI) workflow, which is well suited for exploring such a large parameter space (Fig.3.B). SBI takes as the input a prior probability distribution of the parameters' values, compares simulated and observed data features across several parameter

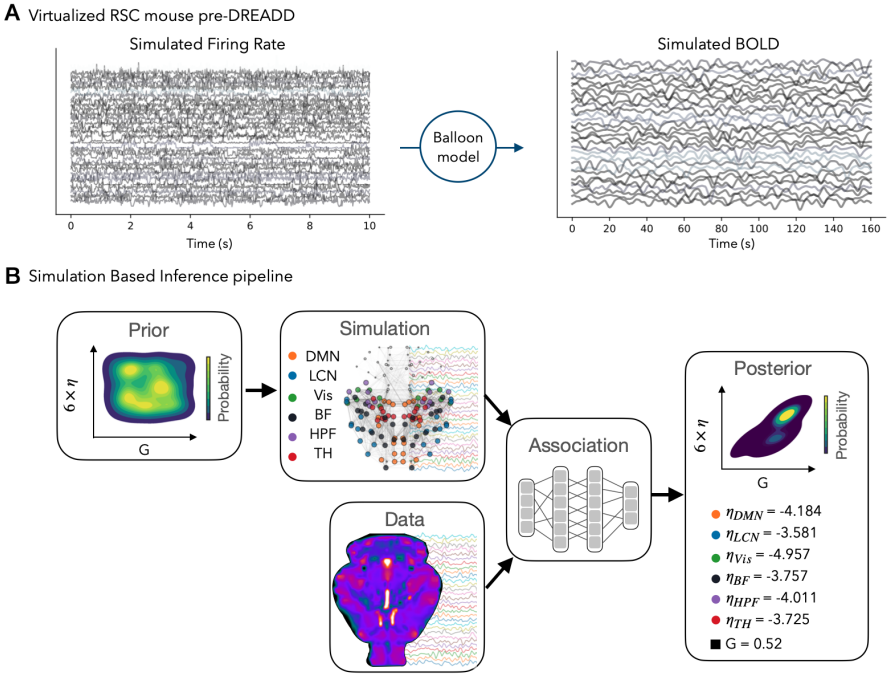

Fig. 3 Virtual Mouse Brain and Simulation-Based Inference: A) The Virtual Mouse Brain pipeline allows the generation of fast neuroelectric (firing rate, left) and slow hemodynamic (BOLD, right) activities in silico. Here we simulated realistic brain activity for the average RSC mouse pre-DREADD. In order to closely match the empirical data features, we need to infer the local and global model parameters. B) The best configuration of model parameters was found by a Simulation-Based Inference (SBI) approach. In short, uniform prior probability distributions of global coupling (G) and regional excitability (6 η values) were given as the pipeline input. Then, a large number of simulations were generated using random parameters taken from the prior distribution. In each simulation, data features were extracted for probabilistic inference against empirical data. Deep neural density estimators were trained to learn the association between simulations and data. Finally, the SBI outputs a posterior probability distribution quantifying the best working point where simulations match observations, with the associated uncertainty in the estimation.

values, and uses a probabilistic deep learning model to output a posterior distribution peaked at a configuration of parameters where the simulations best match the empirical data [21] (see Methods). Importantly, SBI allows for inference on multimodal distributions and parameter degeneracy, as compared to classical variational inference used in Dynamic Causal Modelling [33, 34].

2.5 Connectional diaschisis in silico: BOLD analysis

Having performed parameter estimation to reproduce pre-DREADD activity in the RSC group, we reasoned that if our simulations were to bear any physiological relevance, the focal silencing in silico should produce local and large-scale effects without further parameter manipulation. We first used the working point parameters listed in Fig.3.B, running $N = 264$ baseline

(Base) simulations by changing the initial conditions. We then performed two types of manipulations, manually increasing or decreasing by $\sim 10\%$ the excitability of the (left and right, ventral and dorsal) RSC without changing any other parameter value. We compared the three arrays of simulations whose settings only differed in the excitability value of the retrosplenial cortex: $\eta_{RSC} = \eta_{DMN} = -4.184$ in the simulated pre-silencing (Base), higher excitability $\eta_{RSC} = -3.8$ in the simulated focal excitation (Exc), and lower excitability $\eta_{RSC} = -4.6$ in the simulated focal inhibition (Inh). Despite the local nature of the manipulations, the average BOLD-FC significantly changes at the whole brain level (Fig.4.A, left). If RSC excitability is decreased, FC increases (Fig.4.A, left), in line with experimental results reporting over-connectivity post-DREADD inhibition [16]. Conversely, FC decreases if RSC excitability increases (Fig.4.A, left). In agreement with the results shown in Figure 2.A-B, a decrease in FC was associated with a decreased NDP, and conversely, an increase in FC was associated with increased bursting i.e., larger events in the NDP distribution (Fig.4.A, right). Increased (decreased) FC was associated to a greater (lower) correlation between FC and the Allen Structural Connectivity (SC) (Fig.4.B). FC-SC correlation was identified as a relevant marker of brain function, whereby several pathologies result in deviations from healthy values of the FC-SC correlation [35, 36]. Finally, we compared the simulated data with the empirical BOLD data reconstructed at the ROI level. The delta FCs–defined as the difference between the FC in the case of focal excitation or inhibition, minus the baseline FC_{base} (Fig. 4.C, top)–show that modulating retrosplenial excitability results in a strong effect over DMN and Visual networks and in their connections to the Th network. These results confirm that focal brain manipulations result in large-scale effects.

Since FC decreases in our experimental conditions following focal inactivation, and based on our theoretical results, we predicted that DREADD inhibition and lesion resulted in a paradoxical increase of excitability in the targeted ROIs. The general decrease in delta FC observed for RSC DREADD inhibition (Fig.4.C, bottom right) significantly correlates with the decrease observed for simulated focal excitation (Sperman's $r_s = 0.12, p < 0.001$). The delta FC of the CTRL group shows a weaker correlation ($r_s = 0.05, p < 0.001$). Both delta FC of RSC and CTRL groups anticorrelate with the simulated delta FC in the case of focal inhibition ($r_s = -0.21, p < 0.001$, and $r_s = -0.1, p < 0.001$, respectively). Despite these correlation values being moderate, they are highly significant, and correlations in the RSC group are always higher than in the CTRL group. Furthermore, notice that the inhibited and excited values of the η_{RSC} parameter were not fine-tuned to maximize the correlation values, which was beyond the illustrative scope of this analysis. These results support the theoretical prediction that focal silencing results in an overall increase of excitability in the target region. For a visual comparison of the altered topography after simulated focal excitation, we plot the 1.5 percentile of the strongest decaying long-range correlations (Fig.4.D, top), which can be compared to the strongest decaying edges observed in the RSC (Fig.4.D, bottom).

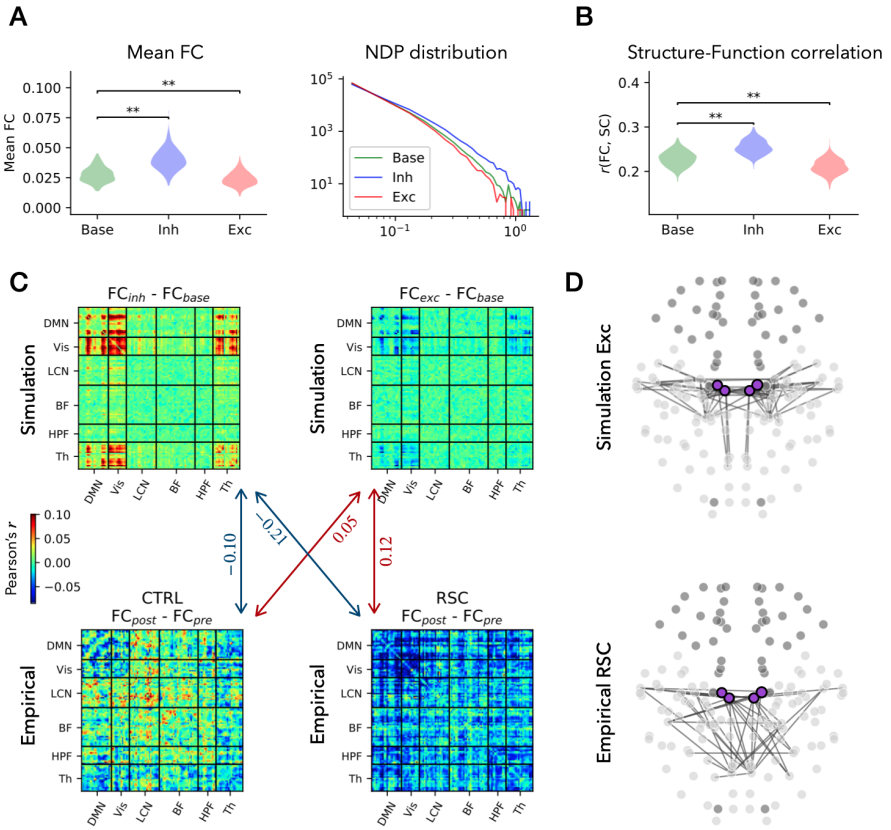

Fig. 4 Connectivity changes after focal excitability modulation in silico: A) The average FC increased after focal inhibition, while it decreased after focal excitation (Wilcoxon test: $p < 0.001$ (*), $p < 0.0001$ (**)). The NDP distribution changed accordingly, with less large bursts associated to decreased FC, and vice versa. B) The Pearson correlation between FC and the Allen SC (used as the structural connectome for the simulations) increased after focal inhibition, while it decreased after focal excitation. C) The simulated FC difference (Exc-Base, or Inh-Base; top row) and the observed FC differences (post-pre; bottom row) for the CTRL and RSC groups. The numbers indicate the Spearman's r_s between two matrices linked by the associated arrow ($p < 0.001$). D) The edges that decreased the most in terms of correlation after simulated RSC excitation (top), and the edges with the largest correlation decrease in the observed RSC group (bottom; decrease larger than any edge in CTRL). Purple nodes mark the left/right, ventral/dorsal RSC.

These simulation results demonstrate connectional diaschisis in silico, allowing us to interpret experimental data, hypothesize the effects of experimental manipulations over cell excitability, and predict the effects of focal excitation and inhibition. After estimating the parameters that enabled to reproduce baseline conditions, we did not perform any further parameter adjustments to fit theoretical and experimental data. Remarkably, our whole-brain simulations produced large-scale effects similar to those found experimentally and generated predictions that we validated experimentally.

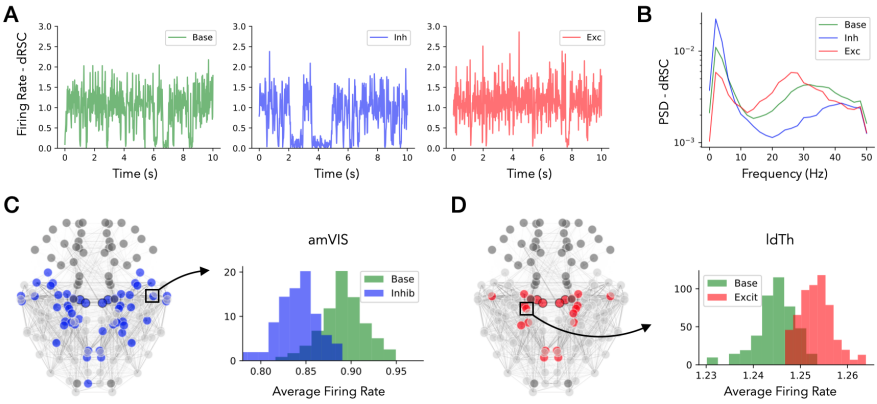

Fig. 5 Diaschisis in silico: A) Firing rate activity for the dorsal RSC (dRSC) in Base, Inh, and Exc simulations. B) The PSD for dRSC shows opposite changes after focal inhibition or excitation. C) RSC inhibition leads to decreased mean firing rate in a distributed network of nodes, such as the anteromedial visual area (amVIS). D) RSC excitation leads to an increased mean firing rate across a distributed subset of ROIs, such as the laterodorsal nucleus of the Thalamus (ldTh).

2.6 Focal diaschisis in silico: Local Field Potential analysis

Brain simulations also allowed us to investigate the neuroelectric activity underlying the BOLD dynamics in each brain region, an analysis that cannot be performed experimentally. Figure 5.A shows the effects of the modulation (inhibition or excitation) of RSC excitability in the left dorsal RSC (dRSC). Power spectral analysis revealed that inhibition of RSC results in increased slow frequencies and decreased fast frequencies (Fig.5.B), in keeping with previous experimental data [16]. The opposite result is predicted to occur (decreased slow frequencies and increased fast frequencies) when the excitability of the RSC is increased (Fig.5.B).

Studying the simulated fast firing rate dynamics, we further show that the activity also changes in brain regions away from the silenced region, therefore demonstrating diaschisis at rest (Fig.5.C-D). In particular, the inhibition of RSC resulted in a significant firing rate decrease in a subnetwork of ROIs (blue nodes in Figure 5.C). An example of firing rate distributions before and after RSC inhibition is shown for the left anteromedial visual cortex (amVIS; Fig.5.C, right). Conversely, increasing excitability of RSC resulted in an increased firing rate in a subset of regions (red nodes in Figure 5.D), such as the right latero-dorsal nucleus of the Thalamus (ldTh; Fig.5.D, right). Importantly, these changes do not involve all brain regions but a subset spanning a distributed and structured network.

Overall, these results demonstrate both focal and connectional diaschisis in silico. Specifically, they predict that modulating the excitability of a brain region produces a large-scale suppression of FC and local changes in firing rate activity in brain areas that are distant from the modulated region.

2.7 Inferring the mechanisms of network reconfiguration following focal region silencing

Our previous analyses did not encompass any parameter estimation of the post-silencing data. However, local manipulations may lead to reorganizations in other brain regions, including their excitability (η) or their connections (G), as typically observed after brain lesions, e.g. after stroke [37] or in epilepsy [38]. We thus used SBI to infer the configurations of local and global parameters that best explain the data features before and after focal intervention in all mouse groups (Fig.6.A). Each violin plot in Figure 6.A represents the distribution of estimated parameters for several subsets of three mice. Namely, within each group (e.g., pre-silencing RSC), we randomly picked three mice and measured an array of average features (e.g., average FC). Then, we ran the SBI pipeline to estimate the working point where the simulations best match the average features of the mice subset. SBI predicts that focal region silencing induces both local and global alterations. Except for the CTRL group, the global coupling G was always decreased after focal silencing (Fig.6.A), indicating a decoupling between structure and function. This result is in line with the analysis in Figure 4.B where the correlation between structure and function decreased after RSC excitability was increased.

Interestingly, the SBI analysis predicts that regional excitability can either decrease or increase after focal silencing (Fig.6.A). In particular, the RSC group presents a significant increase in the excitability of DMN, and in the subcortical HPF, and Th networks. This result extends the previous analyses (Figs.4-5), suggesting the non-trivial possibility of remote changes in excitability [37]. In the ACA group, the excitability of DMN and HPF were increased. In the Th group, excitability increased in DMN, Vis, and Th, whereas it decreased in the LCN.

2.8 Predicting the region where the manipulation occurred from experimental data

Based on the results in Figure 6.A, we hypothesized that silencing a specific site would result in a characteristic pattern of reconfiguration of regional excitability. If this is the case, we should be able to classify the Th, ACA, RSC, and CTRL groups based on the inferred changes in excitability. To test this hypothesis, we defined a six-dimensional array measuring the change in RSNs excitability $\frac{\eta_{pre}-\eta_{post}}{\eta_{pre}+\eta_{post}}$ (Fig. 6.B) for each subset of mice in each group. We used cross-validation to show that mice can be classified according to the effects of silencing on the network excitability. We then performed the cross-validation on 30 triplets of mice per group. In Figure 6.B (right), we show that mice can indeed be classified according to the changes in network excitability as estimated by SBI. Mice in the various groups were classified with 90% accuracy for Th, 53% for ACA, 63% for RSC, and 97% for CTRL. In other words, by providing the data before and after silencing from a non-specified group of mice, SBI enables us to accurately infer to which group the mice belong. The

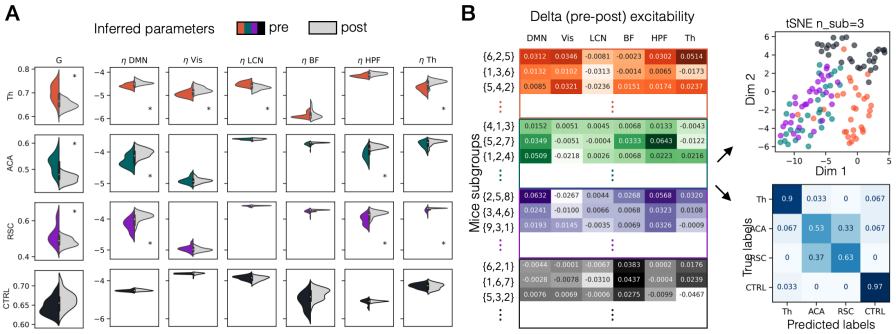

Fig. 6 Local and global reparametrization and silencing classification: SBI was used to infer parameters in both the pre- (colored) and post-silencing (gray) data for each mouse. The violin plots represent the distribution of inferred parameters. SBI predicts both local and global alterations resulting from focal region silencing; the global coupling G always decreases (except CTRL), whereas the local excitability parameter η can either decrease or increase. Significant shifts in the pre/post distributions are measured via the Wilcoxon test ($p < 0.0001$ (*)). B) The delta pre-post excitability was measured for different triplets of mice within each group. Then tSNE in a two-dimensional map is used to classify a given mouse triplet as belonging to a specific group. Based on the inferred delta excitabilities, the confusion matrix illustrates a high value of accuracy in the classification, particularly in Th, and CTRL groups.

ACA and RSC groups were often mixed by the classification algorithm, due to the similarity of effects induced by silencing ACA and RSC, two strongly connected ROIs of the DMN.

3 Discussion

The present study investigates the mechanisms of focal silencing of brain activity, focusing on the impact of lesioning specific thalamic nuclei and chemogenetic silencing of cortical hubs. Our experiments confirm previous observations of decreased Functional Connectivity upon silencing of cortical hubs [18, 39]. Expanding this prior work, we show that structured and widespread reduction in long-range fMRI connectivity also characterizes subcortical thalamic lesions (Figure 1). Studying brain dynamics produced by our manipulations we show that the Functional Connectivity decrease stems from the compromised ability of the brain to sustain large-scale bursts of activity (Figure 2).

While our results are consistent across manipulations and are statistically significant, the direction of the observed functional changes is in contrast with previous reports of paradoxical over-connectivity upon chemogenetic inhibition of the cortical and subcortical areas in mice and non-human primates [16, 17]. Experimental discrepancies in the extension of the manipulated region, and anesthetic combinations used to map these effects may underlie these differences. More broadly, this apparent divergence reveals a complex and nuanced mechanism underlying the reconfiguration of functional connectivity. The outcome of hypo- and hyperconnectivity after focal inhibition may not hold universally.

In order to shed light on the determinants of these divergent results, we employed personalized virtual mouse brain simulations, which allow the simulation of realistic hemodynamic signals and the simultaneous simulation of electrophysiological activity across the whole brain, an endeavor that is not experimentally achievable yet. This approach played a crucial role in deciphering the mechanistic basis of our experimental observations. By simulating the effects of focal manipulations, our model revealed that controlled inhibition leads to over-connectivity of hemodynamic signals, along with decreased firing rate, and increased(decreased) low(high)-frequency in neuroelectric signals (Fig.4-5). These results closely match the observations previously reported in [16, 17, 40]. A similar change in local field potential was also observed in intracranial electroencephalography recordings in humans where a focal lesion was performed by thermocoagulation [11].

Interestingly, the opposite effect was predicted for focal excitation, resulting in a decrease in long-range correlations, which better aligns with our experimental observations (Fig.4). The focal increase in excitation was paralleled by increased firing rate, decreased low frequency, and more robust high frequency in neuroelectric signals (Fig.5). This prediction of our model could be confirmed in future electrophysiology studies on the effects of increased focal excitability. Initial data, seem to support this prediction, as increased excitability in prefrontal regions upon the use of DREADD activators has been shown to reduce fMRI connectivity as well as slow frequency neural coupling (Sastre D et al., 2023)

Our model provides insights into the complex interplay between different neural activity scales and their modulation upon focal interventions, showing in silico the principle of diaschisis [7]. This notion suggests that modulating the excitability of a single region can lead to cascading changes in network dynamics, with broad implications for interpreting the effects of focal interventions. In fact, our simulation revealed that changes in the neuroelectric activity due to local excitability modulation can affect a widespread network of regions, transcending the manipulated area (Fig.5). Furthermore, based on the comparison of experimental data and modeling, we propose that focal silencing induced by DREADD or lesion could provoke remote changes in excitability (Fig.6).

Importantly, our results are in line with previous results showing both local and non-local effects of brain lesions [7]. For example, experiments with rodent models of cortical lesions induced by photo thrombosis, which is evocative of cortex damage induced by stroke, reveal a perilesional reduction in gamma-aminobutyric acid receptor expression, paired with heightened contralesional NMDA receptor expression, signifying a differential excitation/inhibition imbalance in the two hemispheres [41]. In rats, in vivo chronic partial denervation of Schaffer collaterals projecting to hippocampal CA1 cells resulted in a homeostatic increase of CA1 excitability [42].

In humans, increased fMRI activity in motor and non-motor regions has been observed after stroke [43], especially in the contralesional areas [44–46]. These effects were also related to widespread cortical hyperexcitability [37, 47]. This reconfiguration could be explained by a mechanism of increased activation via decreased inhibition in long-range communication [48–50]. Also, stroke can induce changes in stimulus-evoked responses. For example, TMS stimulation revealed a lowered threshold for eliciting motor-evoked potentials and a higher evoked potentials' amplitude in stroke patients [51].

Our model shows that widespread changes in excitability after focal silencing might be paralleled by decoupling between structure and function, as indicated by the significant decrease of global coupling value post-silencing. These results are in line with previous evidence in virtual human brain simulations of the effects of traumatic brain lesions [52]. These changes might drive the increased segregation of brain regions and contribute to alterations in functional connectivity. This introduces a new layer of complexity to our understanding of how focal interventions impact brain-wide network organization.

The implications of our findings extend beyond fundamental neuroscience. The insights gained from this study hold the potential for personalized predictions of the effects of local modulation on brain organization. Such knowledge could be harnessed in the development of targeted interventions [53], tailored neuromodulation therapies, aid in clinical decision-making, and advancements in brain-computer interface technologies.

Despite these contributions, several limitations warrant consideration. In the chemogenetic experiments, DREADD were applied to all neurons, including both excitatory and inhibitory. Thus, the DREADD silencing could lead

to reduced excitation but also dis-inhibition (increasing excitation). We speculate that this factor could lead to a paradoxical change in excitability like the one inferred from the modeling. Future studies using cell-type specific silencing would be needed to clarify this issue. Diaschisis is generally associated with hypometabolism [7], this aspect was not explored in this study. Furthermore, our experiments lack an electrophysiological correlate to confirm the effects of neuronal activity. Our study focused on specific species and brain regions; exploring a broader range of species and regions could offer a more comprehensive understanding.

In conclusion, our study underscores the intricate consequences of focal brain region silencing, providing novel insights into brain function and the implications of localized modulation. By elucidating the interactions between neural scales, excitability changes, and remote effects, this study contributes to a deeper understanding of brain network dynamics and opens avenues for future research in both basic neuroscience and clinical applications.

4 Methods

4.1 Empiric datasets

In two independent experiments, we performed mouse brain imaging before and after region silencing (Fig.1,A).

The 1st dataset was obtained from 9 C57BL6 mice with irreversible lesions in thalamic nuclei induced under ketamine + xylazine (100mg/kg, 10mg/kg) or isoflurane (2.5%) by i.c. injections of NMDA 0.1 M NMDA in autoclaved PB 0.12M using a Nanoject III (Drummond Scientific) with a slow injection rate (0.03μL/min) over 10 min. The glass pipette was retained in place for another 10 min and then slowly retracted. After injection, the wound was closed using Dura-Gel (Cambridge Neurotech) and Metabond (Parnell), then sutured. BOLD rs-fMRI acquisitions were performed before and 6 wk after surgery under light anesthesia (0.6% isoflurane) and sedation (s.c injection of a single dose of medetomidine 0.13 mg/kg) on a 7T Pharmascan Bruker equipped with a cryoprobe using 2D GE-EPI (spatial resolution of $0.167 \times 0.167 \times 0.40\text{mm}^3$; echo time of 16.30 ms; tBOLD Repetition Time TR= 1.75 s, flip angle of 30°, 15 min, 512 repetitions). Data processing (FSL software) included motion correction, regression of the volumes affected by motion and by sudden changes in BOLD signal intensity, skull stripping, bias field correction, slice timing correction, grand-mean intensity normalization, band pass filtering ($0.01-0.1$Hz), registration to Allen Template using linear and nonlinear transformations and spatial smoothing with a Gaussian Kernel of 4 mm (= 0.4mm in original resolution)[54, 55]. 3 mice were excluded since they did not present evident lesions from histology experiments, or because artifacts were present in the fMRI activity.

The 2nd dataset was obtained by DREADD inhibition of the retrosplenial cortex (RSC; N = 14) or anterior cingulate area (ACA; N = 7) on C57Bl/6J male mice, which are generally considered functional hubs in the mouse brain

[18, 32]. Another control group (N = 8) was also included in which a control virus was injected into RSC. As RSC is a very elongated area, we targeted the posterior section based on our preliminary study which shows stronger functional connectivity within DMN. Surgeries were performed at least one month before fMRI. The animal (10 – 16 weeks of age) was anesthetized with $1.5 - 2\%$ isoflurane during surgery. Enrofloxacin (6 mg/kg) and carprofen (5 mg/kg) were injected subcutaneously to prevent infection and relieve pain and inflammation, respectively. Body temperature was maintained at 37 °C with a heating pad. In ACA and RSC groups, inhibitory DREADD virus AAV2/1 pSyn-hM4D(Gi)-T2A-mScarlet was bilaterally injected into ACA or RSC with 0.25 µL for each side. In the CTRL group, control virus AAV DJ/8 pAM-tdTomato was bilaterally injected into RSC with 0.25 µL for each side. Both DREADD and control viruses were obtained from Sah lab, Queensland Brain Institute, The University of Queensland, QLD, Australia. The relative coordinates to Bregma of ACA and RSC based on Paxions and Franklin Mouse Brain atlas, fifth edition are:

- Anterior cingulate area (ACA). ML: ±0.3mm; AP: +0.4mm; DV: -0.9mm.
- Retrosplenial cortex (RSC). ML: ±0.4mm; AP: -2.7mm; DV: -0.6mm.

The virus was injected using a Nanoject III (Drummond Scientific) with a slow injection rate (0.03 μL/min) over 10 min. The glass pipette was retained in place for another 6 min and then slowly retracted. After injection, the wound was closed using Vetbond (3M) and sutured. Enrofloxacin and carprofen were administered for another two days. Animals were kept in their home cage (group housing of 2-4 animals per cage) for 4 weeks to recover and to allow expression of the virus before MRI. MRI was conducted on a 9.4 T system (BioSpec 94/30, Bruker BioSpin MRI GmbH). Animals were initially anesthetized using 3% isoflurane in a 2:1 air and oxygen mixture. After being secured in an MRI-compatible holder using custom-made tooth and ear bars, a bolus of medetomidine was delivered via an i.p. catheter (0.05-0.1 mg/kg), and the isoflurane level was progressively reduced to $0.25 - 0.5\%$ over 10 min, after which sedation was maintained by a constant i.p. infusion of medetomidine (0.1mg/kg/h). Key physiological parameters, including arterial oxygenation saturation (SpO2), rectal temperature, heart rate, and respiratory rate, were measured by an MRI-compatible monitoring system (SAII Inc). Body temperature was maintained at 36.5°C with a heated water bath. About 45min after the bolus injection of medetomidine, the first 10 min resting-state fMRI data was acquired using multiband EPI as a pre-DREADD scan (TR/TE = 300/15 ms, thickness = 0.5 mm, gap = 0.1 mm, 16 axial slices covering the whole cerebrum with in-plane resolution of 0.3 × 0.3 mm2) [56]. After this, 1mg/kg water-soluble clozapine N-oxide (CNO dihydrochloride; cat #6329, Tocris Bioscience) was slowly injected via a pre-implanted catheter (i.p.) in 1 min. 30 min after the CNO injection, another 10 min resting-state fMRI was performed as a post-DREADD scan. The data was preprocessed by motion correction, distortion correction, nuisance removal [57], bandpass filter (0.010.3Hz), transformed

to ABA 200μm template with 10x resolution (2mm) and then smoothed by 6mm Gaussian (= 0.6mm in original resolution).

For region-level analysis, both datasets were registered onto a parcellation of the Allen Mouse brain consisting of $N = 148$ regions of interest (ROIs).

4.2 Empiric structural connectivity

The connectome used in the simulations was obtained by employing The Virtual Mouse Brain pipeline (TVMB; [20]) on tracer experiments performed at the Allen Institute ([27]). In these experiments, adult male C57Bl/6J mice were locally injected with a recombinant adeno-associated virus expressing the EGFP anterograde tracer. The tracer migration signal was captured using a serial two-photon tomography system, providing information about the axonal projections originating from the injected sites. Injection density was defined as the ratio of infected pixels to the total number of pixels in the source region. Similarly, projection density was defined in each target region as the ratio of detected pixels following injections in the source region to the total number of pixels in the target region. By averaging injection experiments conducted in the right brain areas and targeting regions in both the ipsilateral and contralateral hemispheres, a tracer-based connectome was constructed. Structural connection strength between a source region n and a target region m (referred to as the link nm) was determined by calculating the ratio of the projection density at region m to the injection density at region n. The resulting tracer connectome displayed normalized links ranging between 0 and 1.

4.3 Neural mass model

In whole-brain simulations, the activity of each ROI is modeled by suitable dynamical equations describing the mean-field behavior of an isolated neural mass. In this work, we used a neural mass model (NMM) which describes the co-evolution of mean firing rate r and mean membrane potential V of a large population of all-to-all coupled quadratic integrate and fire (QIF) neurons [58]. The local region n dynamics is described by the following NMM equations

$$\tau_c \dot{r_n} = \frac{\Delta}{\pi} + 2 r_n V_n, \tag{1}$$

$$\tau_c \dot{V_n} = V_n^2 + \eta + J r_n - \pi^2 r_n^2 + I_n. \tag{2}$$

Here we used default parameters $\eta = -4.6$ for the average excitability of the QIF neurons, $\Delta = 0.7$ for the spread of the neuronal excitability distribution in the population, $J = 14.5$ for the synaptic weight across coupled QIF neurons, and $\tau_c = 1$ for the characteristic time. In this configuration, the decoupled neural mass model is in a bistable regime [29], with a UP state corresponding to a stable focus and a DOWN state corresponding to a fixed point. The input I_n is additive in the membrane potential equation.

4.4 Virtual brain simulations

Connecting the NMM equations of each brain region through the Allen structural connectome defines a system of coupled equations that models the mouse brain dynamics. When a region n is coupled to other brain regions through the structural connectivity matrix W_{nm}, the total input to region n is

$$I_n = G \sum_{m \neq n} W_{nm} r_m \tag{3}$$

The global coupling parameter G regulates the influence of the connectome over the local dynamics. When $G = 0$ the regions are decoupled and the brain regions evolve according to the local NMM dynamics. The more G increases, the more the brain regions' dynamics are intertwined. In this work, we do not account for signal transmission delays, and we do not simulate excitatory versus inhibitory population dynamics (see limitations in Discussion. The solution of the coupled system was obtained by numerical integration using the TVMB platform [19, 20], and corresponds to a simulated dataset describing the evolution of the $2N$ variables $(r_n(t), V_n(t))$. The sampling rate of these neuroelectric variables is set to 1000Hz. The simulated BOLD activity $B_n(t)$ in each region is derived by filtering the firing rate $r_n(t)$ through the Balloon-Windkessel model [59], modeling the hemodynamic response function of the BOLD signal. The parameters were tuned to match realistic hemodynamic timescales for the mouse (Suppl.Fig.5). We use a repetition time of 2 seconds so that the BOLD rate is 0.5 Hz.

4.5 Simulation-based inference (SBI)

Bayes' rule describes how the prior (background information before seeing the data) is combined with likelihood (available information in the data) to form the posterior distribution for making probabilistic inferences and predictions [60]. Mathematically speaking, the posterior distribution of parameters θ given the model m is $p(\theta \mid y, m) \propto p(y \mid \theta, m)p(\theta \mid m)$, which $p(y \mid \theta, m)$ represents the likelihood and $p(\theta \mid m)$ is the prior information [61]. For many high-dimensional and nonlinear dynamical models, such as The Virtual Mouse Brain (TVMB) used in this study, the calculation of the likelihood function becomes intractable [34], and standard methods, such as Markov chain Monte Carlo sampling, cannot be applied directly to carry out Bayesian inference. Hence, likelihood approximation algorithms such as Simulation-based Inference (SBI; [21]) are required to efficiently estimate the posterior of the unknown parameters. To perform SBI without sensitivity to a distance measure for model evaluation [62], deep neural density estimators can be trained on a set of forward simulations (generated with random parameters drawn from a prior), to learn the likelihood function. In particular, using invertible transformations through Masked Autoregressive Flow (MAF; [63]) in a class of SBI methods (the so-called Sequential neural posterior estimators, SNPE; [64]), we are able to readily estimate the approximated posterior

$q_\phi(\theta \mid y, m)$ with learnable parameters ϕ, so that for the observed data y_{obs}: $q_\phi(\theta \mid y_{obs}, m) \simeq p(\theta \mid y_{obs}, m)$.

In this study, we ran a MAF in one round of SNPE, with 5 autoregressive layers, each with two hidden layers of 50 units, as implemented in the PyTorch-based SBI package [65]. To estimate the joint posterior distribution between parameters G, and η, we performed 10^5 simulations with a uniform prior as $G \in \mathcal{U}(0, 1.1)$ and $\eta_i \in \mathcal{U}(-6, -3.5)$.For the training of the neural network, we utilized features extracted from the BOLD signal. These features were related to static and dynamic network measures: the Functional Connectivity (FC) was measured as the pairwise Pearson's correlation among ROIs-level signals; the dynamic Functional Connectivity (dFC) is a (time$\times$ time) matrix defined as the Pearcon's correlation among pairs of instantaneous co-activation patterns $E_{ij}(t_A) \cdot E_{ij}(t_B)$ (vertical slices of the green block in Figure 2.A) at times t_A and t_B. The features used in the training included the fluidity (i.e., the variance of dFC), the overall sum of FC and dFC matrices, the average value of FC homotopic, and the variance of the masked dFC matrix over six sub-networks: DMN (Default Mode Network), Vis-Aud (Visual-Auditory), LCN (Limbic-Cortical Network), BF (Basal Forebrain), HPF (High-Processing Frontal), and Thalamus.

4.6 Surrogate data

In order to compare our results in 2 a with the null hypotheses of random evolution and of inter-regional stationarity of the data, we build phase-randomized surrogates. According to [66] the phase randomized surrogate is obtained by adding a uniformly distributed random phase to each frequency of the Fourier-transformed signal, and subsequently retrieving the phase-randomized signals by inverse Fourier transform. Importantly, the phase shift is different in every frequency but can be applied uniformly to all the brain regions (cross-spectrum preserved) or separately in every region (cross-spectrum not preserved). Only in the first case, the static FC is preserved. The coherent fluctuations around the stationary FC, however, are destroyed. For more details see also [67].

References

[1] Roth, B. L. Dreadds for neuroscientists. *Neuron* **89** (4), 683–694 (2016) .

[2] Yizhar, O., Fenno, L. E., Davidson, T. J., Mogri, M. & Deisseroth, K. Optogenetics in neural systems. *Neuron* **71** (1), 9–34 (2011) .

[3] Thiebaut de Schotten, M. & Forkel, S. J. The emergent properties of the connected brain. *Science* **378** (6619), 505–510 (2022) .

[4] Steinmetz, N. A., Zatka-Haas, P., Carandini, M. & Harris, K. D. Distributed coding of choice, action and engagement across the mouse brain. *Nature* **576** (7786), 266–273 (2019) .

[5] Marshel, J. H. *et al.* Cortical layer–specific critical dynamics triggering perception. *Science* **365** (6453), eaaw5202 (2019) .

[6] from Monakov, C. *Localization in the cerebrum and degradation of function by cortical foci* (JF Bergman, 1914).

[7] Carrera, E. & Tononi, G. Diaschisis: past, present, future. *Brain* **137** (9), 2408–2422 (2014) .

[8] Feeney, D. M. & Baron, J.-C. Diaschisis. *Stroke* **17** (5), 817–830 (1986) .

[9] Assenza, G., Zappasodi, F., Pasqualetti, P., Vernieri, F. & Tecchio, F. A contralesional eeg power increase mediated by interhemispheric disconnection provides negative prognosis in acute stroke. *Restorative Neurology and Neuroscience* **31** (2), 177–188 (2013) .

[10] Tecchio, F. *et al.* Outcome prediction in acute monohemispheric stroke via magnetoencephalography. *Journal of neurology* **254**, 296–305 (2007) .

[11] Russo, S. *et al.* Focal lesions induce large-scale percolation of sleep-like intracerebral activity in awake humans. *NeuroImage* **234**, 117964 (2021) .

[12] Mohajerani, M. H., Aminoltejari, K. & Murphy, T. H. Targeted mini-strokes produce changes in interhemispheric sensory signal processing that are indicative of disinhibition within minutes. *Proceedings of the National Academy of Sciences* **108** (22), E183–E191 (2011) .

[13] Gratton, C., Nomura, E. M., Pérez, F. & D'Esposito, M. Focal brain lesions to critical locations cause widespread disruption of the modular organization of the brain. *Journal of cognitive neuroscience* **24** (6), 1275–1285 (2012) .

[14] Mohajerani, M. H., McVea, D. A., Fingas, M. & Murphy, T. H. Mirrored bilateral slow-wave cortical activity within local circuits revealed by fast bihemispheric voltage-sensitive dye imaging in anesthetized and awake mice. *Journal of Neuroscience* **30** (10), 3745–3751 (2010) .

[15] Redecker, C., Wang, W., Fritschy, J.-M. & Witte, O. W. Widespread and long-lasting alterations in gabaa-receptor subtypes after focal cortical infarcts in rats: mediation by nmda-dependent processes. *Journal of Cerebral Blood Flow & Metabolism* **22** (12), 1463–1475 (2002) .

[16] Rocchi, F. *et al.* Increased fmri connectivity upon chemogenetic inhibition of the mouse prefrontal cortex. *Nature communications* **13** (1), 1056 (2022) .

[17] Elorette, C. *et al.* The neural basis of resting-state fmri functional connectivity in fronto-limbic circuits revealed by chemogenetic manipulation. *bioRxiv* 2023–06 (2023) .

[18] Peeters, L. M. *et al.* Chemogenetic silencing of neurons in the mouse anterior cingulate area modulates neuronal activity and functional connectivity. *Neuroimage* **220**, 117088 (2020) .

[19] Sanz-Leon, P., Knock, S. A., Spiegler, A. & Jirsa, V. K. Mathematical framework for large-scale brain network modeling in the virtual brain. *Neuroimage* **111**, 385–430 (2015) .

[20] Melozzi, F., Woodman, M. M., Jirsa, V. K. & Bernard, C. The virtual mouse brain: a computational neuroinformatics platform to study whole mouse brain dynamics. *Eneuro* **4** (3) (2017) .

[21] Cranmer, K., Brehmer, J. & Louppe, G. The frontier of simulation-based inference. *Proceedings of the National Academy of Sciences* **117** (48), 30055–30062 (2020). URL https://www.pnas.org/doi/abs/10.1073/pnas.1912789117. https://doi.org/10.1073/pnas.1912789117 .

[22] Hashemi, M. *et al.* The bayesian virtual epileptic patient: A probabilistic framework designed to infer the spatial map of epileptogenicity in a personalized large-scale brain model of epilepsy spread. *NeuroImage* **217**, 116839 (2020). URL https://www.sciencedirect.com/science/article/pii/S1053811920303268. https://doi.org/https://doi.org/10.1016/j.neuroimage.2020.116839 .

[23] Hashemi, M. *et al.* Amortized bayesian inference on generative dynamical network models of epilepsy using deep neural density estimators. *Neural Networks* **163** (2023). URL https://www.sciencedirect.com/science/article/pii/S0893608023001752. https://doi.org/https://doi.org/10.1016/j.neunet.2023.03.040 .

[24] Rubinov, M. & Sporns, O. Weight-conserving characterization of complex functional brain networks. *Neuroimage* **56** (4), 2068–2079 (2011) .

[25] Cole, M. W., Pathak, S. & Schneider, W. Identifying the brain's most globally connected regions. *Neuroimage* **49** (4), 3132–3148 (2010) .

[26] Gozzi, A. & Schwarz, A. J. Large-scale functional connectivity networks in the rodent brain. *Neuroimage* **127**, 496–509 (2016) .

[27] Oh, S. W. *et al.* A mesoscale connectome of the mouse brain. *Nature* **508** (7495), 207–214 (2014) .

[28] Zamani Esfahlani, F. *et al.* High-amplitude cofluctuations in cortical activity drive functional connectivity. *Proceedings of the National Academy of Sciences* **117** (45), 28393–28401 (2020) .

[29] Rabuffo, G., Fousek, J., Bernard, C. & Jirsa, V. Neuronal cascades shape whole-brain functional dynamics at rest. *Eneuro* **8** (5) (2021) .

[30] Gutierrez-Barragan, D., Basson, M. A., Panzeri, S. & Gozzi, A. Infraslow state fluctuations govern spontaneous fmri network dynamics. *Current Biology* **29** (14), 2295–2306 (2019) .

[31] Pope, M., Fukushima, M., Betzel, R. F. & Sporns, O. Modular origins of high-amplitude cofluctuations in fine-scale functional connectivity dynamics. *Proceedings of the National Academy of Sciences* **118** (46), e2109380118 (2021) .

[32] Liska, A., Galbusera, A., Schwarz, A. J. & Gozzi, A. Functional connectivity hubs of the mouse brain. *Neuroimage* **115**, 281–291 (2015) .

[33] Friston, K. J., Harrison, L. & Penny, W. Dynamic causal modelling. *Neuroimage* **19** (4), 1273–1302 (2003) .

[34] Hashemi, M. *et al.* Amortized bayesian inference on generative dynamical network models of epilepsy using deep neural density estimators. *Neural Networks* **163**, 178–194 (2023) .

[35] Zimmermann, J., Griffiths, J., Schirner, M., Ritter, P. & McIntosh, A. R. Subject specificity of the correlation between large-scale structural and functional connectivity. *Network Neuroscience* **3** (1), 90–106 (2018) .

[36] Wang, Z., Dai, Z., Gong, G., Zhou, C. & He, Y. Understanding structural-functional relationships in the human brain: a large-scale network perspective. *The Neuroscientist* **21** (3), 290–305 (2015) .

[37] Bütefisch, C. M., Netz, J., Wessling, M., Seitz, R. J. & Hömberg, V. Remote changes in cortical excitability after stroke. *Brain* **126** (2), 470–481 (2003) .

[38] Badawy, R. A., Loetscher, T., Macdonell, R. A. & Brodtmann, A. Cortical excitability and neurology: insights into the pathophysiology. *Functional neurology* **27** (3), 131 (2012) .

[39] Tu, W., Ma, Z. & Zhang, N. Brain network reorganization after targeted attack at a hub region. *NeuroImage* **237**, 118219 (2021) .

[40] Roelofs, T. J. *et al.* A novel approach to map induced activation of neuronal networks using chemogenetics and functional neuroimaging in rats: A proof-of-concept study on the mesocorticolimbic system. *Neuroimage* **156**, 109–118 (2017) .

[41] Schiene, K. *et al.* Neuronal hyperexcitability and reduction of gabaa-receptor expression in the surround of cerebral photothrombosis. *Journal of Cerebral Blood Flow & Metabolism* **16** (5), 906–914 (1996) .

[42] Dinocourt, C., Aungst, S., Yang, K. & Thompson, S. M. Homeostatic increase in excitability in area ca1 after schaffer collateral transection in vivo. *Epilepsia* **52** (9), 1656–1665 (2011) .

[43] Rehme, A. K. & Grefkes, C. Cerebral network disorders after stroke: evidence from imaging-based connectivity analyses of active and resting brain states in humans. *The Journal of physiology* **591** (1), 17–31 (2013) .

[44] Weiller, C., Chollet, F., Friston, K. J., Wise, R. J. & Frackowiak, R. S. Functional reorganization of the brain in recovery from striatocapsular infarction in man. *Annals of Neurology: Official Journal of the American Neurological Association and the Child Neurology Society* **31** (5), 463–472 (1992) .

[45] Ward, N., Brown, M., Thompson, A. & Frackowiak, R. Neural correlates of motor recovery after stroke: a longitudinal fmri study. *Brain* **126** (11), 2476–2496 (2003) .

[46] Grefkes, C. & Fink, G. R. Reorganization of cerebral networks after stroke: new insights from neuroimaging with connectivity approaches. *Brain* **134** (5), 1264–1276 (2011) .

[47] Buchkremer-Ratzmann, I. & Witte, O. W. Extended brain disinhibition following small photothrombotic lesions in rat frontal cortex. *Neuroreport* **8** (2), 519–522 (1997) .

[48] Logothetis, N. K., Pauls, J., Augath, M., Trinath, T. & Oeltermann, A. Neurophysiological investigation of the basis of the fmri signal. *nature* **412** (6843), 150–157 (2001) .

[49] Liepert, J., Gorsler, A., van Eimeren, T., Münchau, A. & Weiller, C. Motor excitability in a patient with a somatosensory cortex lesion. *Clinical Neurophysiology* **114** (6), 1003–1008 (2003). URL https://www.sciencedirect.com/science/article/pii/S1388245703000622. https://doi.org/https://doi.org/10.1016/S1388-2457(03)00062-2 .

[50] Blicher, J. U., Jakobsen, J., Andersen, G. & Nielsen, J. F. Cortical Excitability in Chronic Stroke and Modulation by Training: A

TMS Study. *Neurorehabilitation and Neural Repair* **23** (5), 486–493 (2009). URL https://doi.org/10.1177/1545968308328730. https://doi.org/10.1177/1545968308328730, pMID: 19221005, https://arxiv.org/abs/https://doi.org/10.1177/1545968308328730 .

[51] Hallett, M. Transcranial magnetic stimulation: a primer. *Neuron* **55** (2), 187–199 (2007) .

[52] Falcon, M. I. *et al.* Functional mechanisms of recovery after chronic stroke: modeling with the virtual brain. *Eneuro* **3** (2) (2016) .

[53] Falcon, M. I., Jirsa, V. & Solodkin, A. A new neuroinformatics approach to personalized medicine in neurology: The virtual brain. *Current opinion in neurology* **29** (4), 429 (2016) .

[54] Bajic, D., Craig, M. M., Mongerson, C. R., Borsook, D. & Becerra, L. Identifying rodent resting-state brain networks with independent component analysis. *Frontiers in Neuroscience* **11**, 685 (2017) .

[55] Lokossou, H. A. *et al.* Impact of day-night cycle on functional brain connectome in mice. *in review, available at https://archive.ismrm.org/2022/1826.html* (2023) .

[56] Lee, H.-L., Li, Z., Coulson, E. J. & Chuang, K.-H. Ultrafast fmri of the rodent brain using simultaneous multi-slice epi. *Neuroimage* **195**, 48–58 (2019) .

[57] Chuang, K.-H. *et al.* Evaluation of nuisance removal for functional mri of rodent brain. *Neuroimage* **188**, 694–709 (2019) .

[58] Montbrió, E., Pazó, D. & Roxin, A. Macroscopic description for networks of spiking neurons. *Physical Review X* **5** (2), 021028 (2015) .

[59] Friston, K. J., Mechelli, A., Turner, R. & Price, C. J. Nonlinear responses in fmri: the balloon model, volterra kernels, and other hemodynamics. *NeuroImage* **12** (4), 466–477 (2000) .

[60] van de Schoot, R. *et al.* Bayesian statistics and modelling. *Nature Reviews Methods Primers* **1** (1), 1 (2021) .

[61] Hashemi, M. *et al.* The bayesian virtual epileptic patient: A probabilistic framework designed to infer the spatial map of epileptogenicity in a personalized large-scale brain model of epilepsy spread. *NeuroImage* **217**, 116839 (2020) .

[62] Beaumont, M. A. Approximate bayesian computation. *Annual review of statistics and its application* **6**, 379–403 (2019) .

[63] Papamakarios, G., Pavlakou, T. & Murray, I. Masked autoregressive flow for density estimation. *Advances in neural information processing systems* **30** (2017) .

[64] Gonçalves, P. J. *et al.* Training deep neural density estimators to identify mechanistic models of neural dynamics. *Elife* **9**, e56261 (2020) .

[65] Tejero-Cantero, A. *et al.* sbi: A toolkit for simulation-based inference. *Journal of Open Source Software* **5** (52), 2505 (2020). https://doi.org/10.21105/joss.02505 .

[66] Hindriks, R. *et al.* Can sliding-window correlations reveal dynamic functional connectivity in resting-state fmri? *Neuroimage* **127**, 242–256 (2016) .

[67] Prichard, D. & Theiler, J. Generating surrogate data for time series with several simultaneously measured variables. *Physical review letters* **73** (7), 951 (1994) .

[68] Lambers, H. *et al.* A cortical rat hemodynamic response function for improved detection of bold activation under common experimental conditions. *Neuroimage* **208**, 116446 (2020) .

5 Acknowledgments

Funding: This research was supported by the European Union's Horizon 2020 research and innovation program under grant agreement 945539 (SGA3) Human Brain Project and by grant agreement No. 826421 Virtual Brain Cloud. CB received support from the Agence Nationale de la recherche projects ANR-17-CE37-0001-01 and ANR-20-NEUC-0005-02 and ANR-17-CE37-0001-03, France Life Imaging (grant ANR-11-INBS-0006).

Author contributions: G.R, C.B, designed research; G.R., performed research; G.R., A.ZM., M.H., P.V., A.R., simulated the models and analyzed the results; HA.L., Z.L., P.Q., A.Gh., O.A., M.E., KH.C., AT.PB., A.V., performed the experiments; HA.L., Z.L., G.R., AT.PB., A.V., KH.C., preprocessed the experimental data; G.R, P.S., A.Go., V.J., C.B, organized the results; G.R., designed the figures; G.R., P.S., A.Go., V.J., C.B., wrote the paper. X.X contributed equally to this work as the last author. Correspondence should be addressed to Giovanni Rabuffo at giovanni.rabuffo@univ-amu.fr or xxx at xxx@univ-amu.fr.

Competing interests: Authors declare that they have no competing interests.

Data and materials availability: All data, code, and materials used in the analyses will be made available at a GitHub repository depending on the outcome of the editorial process.

Supplementary information for

Inferring the mechanisms of resting-state network reconfiguration upon focal region silencing

Correspondence: giovanni.rabuffo@univ-amu.fr ; viktor.jirsa@univ-amu.fr; christophe.bernard@univ-amu.fr

This PDF file includes:

Fig. S1-5 Appendix A Appendix B

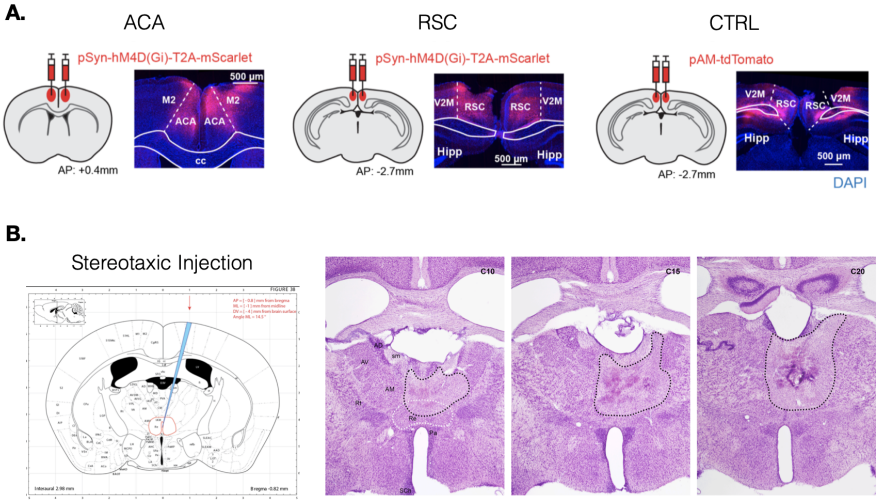

Fig. S1 DREADD virus expression and thalamic lesions.: (A) DREADD expression in ACA, RSC, and CTRL groups. In each subgraph, the left image shows the injection location of the inhibitory DREADD (AAV-pSyn-hM4D(Gi)-T2A-mScarlet) or control (pAM-tdTomato) virus, and the right image shows the fluorescence imaging together with the DAPI staining (blue). cc, corpus callosum; ACA, anterior cingulate area; Hipp, hippocampus; M2, secondary motor cortex; RSC, retrosplenial cortex; V2M, the medial secondary visual cortex. (B) Example of stereotaxic injection in the thalamic lesion data and histology

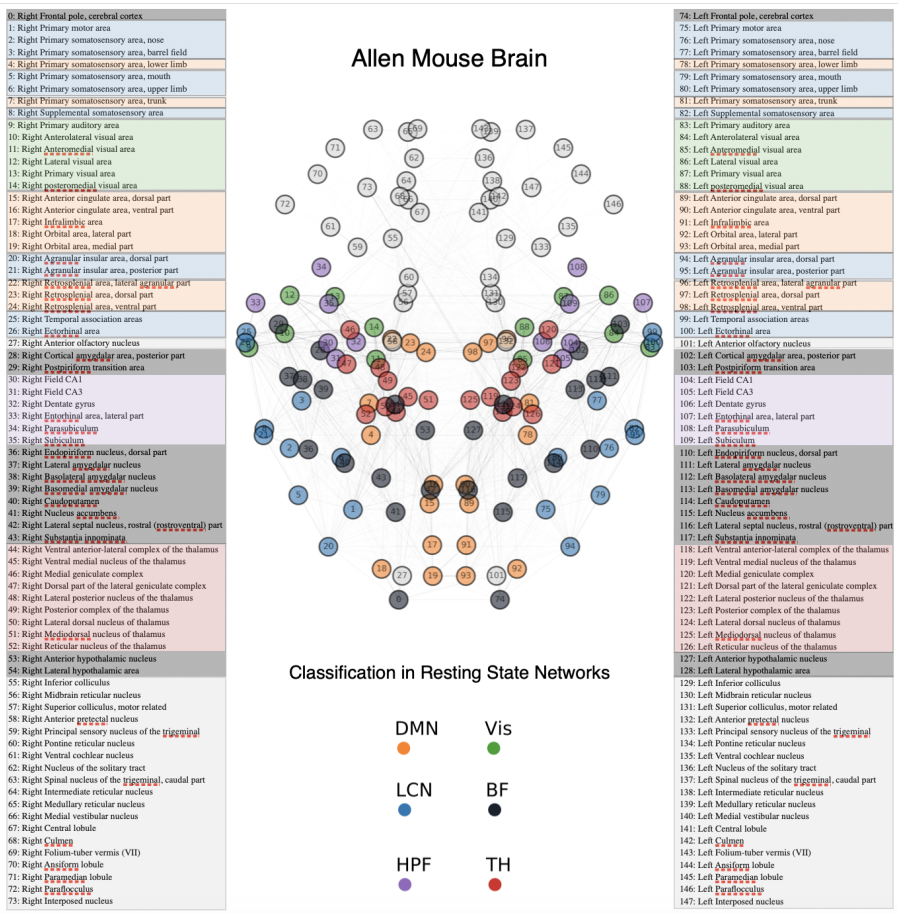

Fig. S2 Allen Mouse Brain parcellation: This parcellation was obtained by processing the Allen Mouse data [27] as in [20].

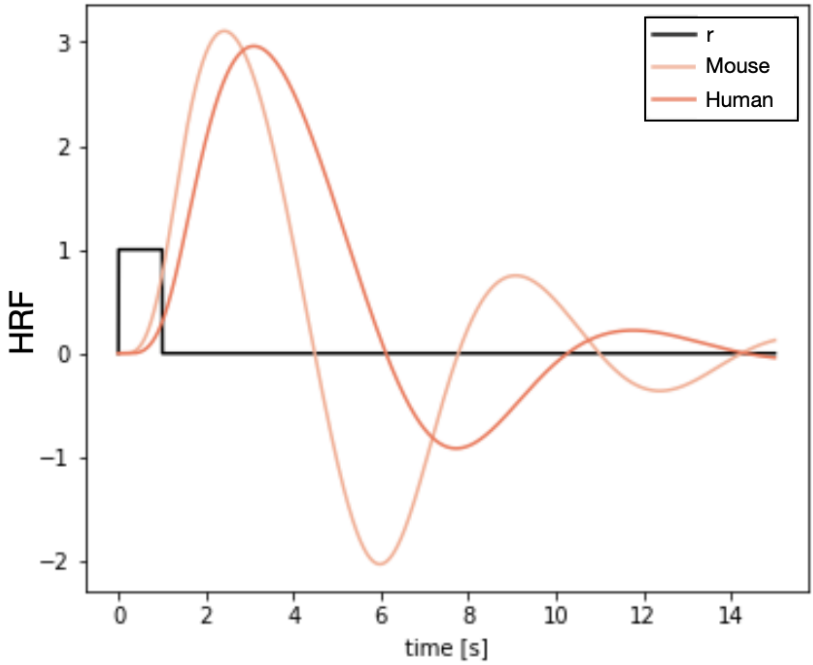

Fig. S3 BOLD Hemodynamic Response Function: For a pulse of the firing rate r the TVB default hemodynamic response function (HRF) for the human is shown. We modified this kernel to match more realistic timescales observed in rodents [68]. The HRF is used to transform simulated firing rates into simulated BOLD data.

5.1 Appendix A: ROIs-level FC analysis

We reconstructed ROIs-level BOLD signals according to an Allen parcellation with $N = 148$ ROIs. We computed FC correlation matrices Supp.Fig.3.A and we organized brain regions in mouse resting-state networks identified according to a common classification (as in Supp.Fig.2): Default Mode Network (DMN), Lateral Cortical Network (LCN), Visual Network (Vis), Basal-Frontal Network (BF), Hippocampal Formation (HPF), and Thalamus (TH). Averaging FC blocks (i.e., edges within black lines in Supp.Fig.3.A), we measured the average FC within and across resting state networks. Comparing pre- and post-silencing for RSC group shows that all inter- and intra- network FC connections decreased after the chemogenetic silencing (Supp.Fig.3.B, matrix numbers mark the result of Wilcoxon test, up/down arrow marks increased/decreased FC, color indicates p-value). The RSC group showed the largest FC decrease. The same procedure applied to ACA group showed a significant decrease only in the FC across LCN and DMN connections, whereas in the Th group, only the correlations across LCN and Vis decreased significantly (Supp.Fig.3.B). The FC decrease for each RSC mouse was measured by $\Delta FC = FC_{post} - FC_{pre}$ Supp.Fig.3.C and it was significant across most brain networks when compared to the CTRL group (Supp.Fig.3.D; Mann-Whitney U test, FDR corrected). Thus, also at the (ROIs-reconstructed) edge level, the values of the observed differences in the RSC group are greater than those in the CTRL group.

The deltas $FC_{post} - FC_{pre}$ were averaged across subjects within the corresponding group (Supp.Fig.3.C). To provide a topography of the differences we selected all edges in the RSC group that showed greater differences than the highest difference observed in the CTRL group (Supp.Fig.3.C). The resulting network is shown in Supp.Fig.3.E. For ACA and Th groups, we show the same number of edges with the highest differences (Supp.Fig.3.E, center, and right, respectively). While silencing RSC and ACA resulted in a suppression of functional networks connected to ACA and RSC, the Thalamic lesions mainly decoupled the interhemispheric connections, with a decrease in correlation between homotopical regions and weaker effects on Thalamic nuclei.

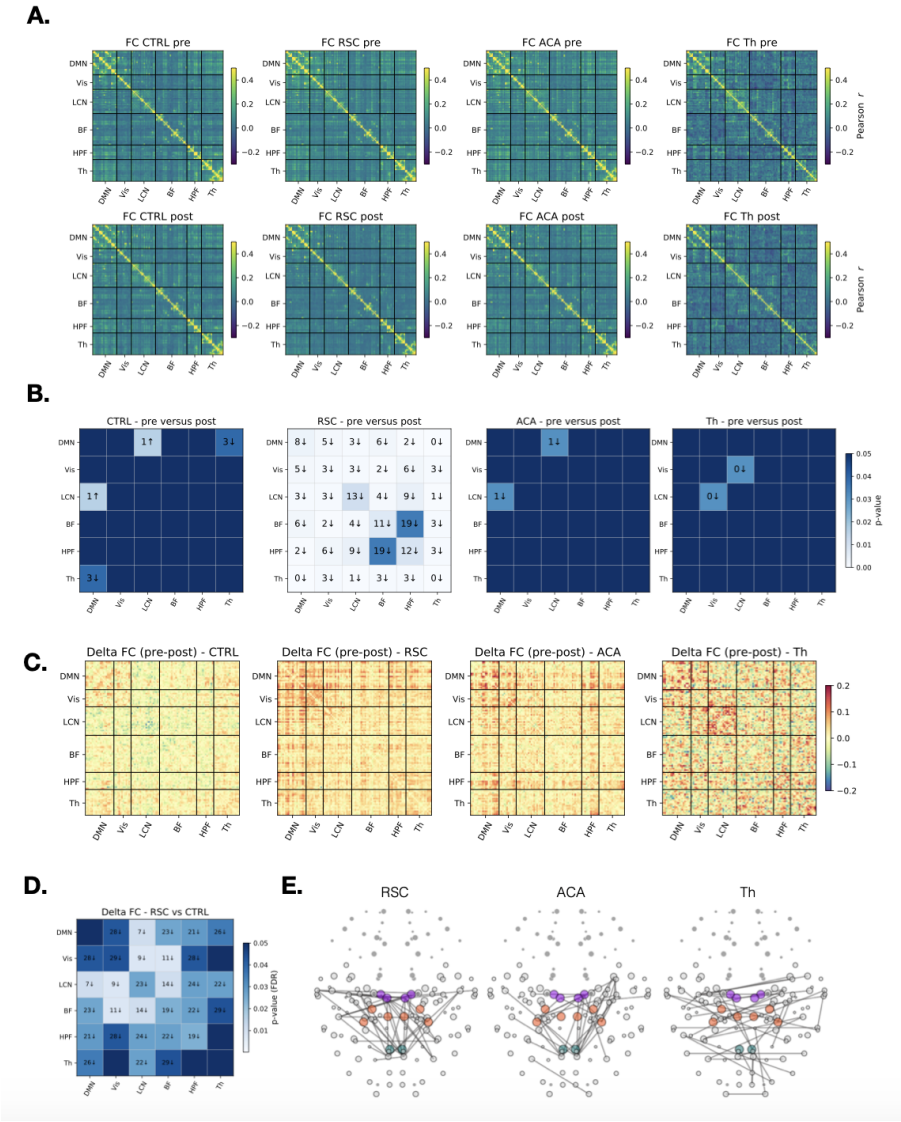

Fig. S4 Region-level Functional Connectivity changes after focal silencing: A) FC at the ROI-level was measured in all mice for pre- and post-silencing trials. ROIs were sorted according to resting state network (RSN) classification (see Methods). B) FC was averaged within and across RSNs (blocks delimited by black lines in panel A), and the statistical significance of the FC decrease was assessed in the RSC group by comparing pre- and post-FC values. B) Each matrix shows the significance of all intra- and inter-RSN changes. In each entry, the numbers indicate the value of the Wilcoxon test, the color indicates the p-value, and the arrows (all pointing down) indicate that correlations within or across RSN always decreased after the focal silencing of RSC. C) Average delta (post-pre) FC in the CTRL, RSC, ACA, and Th groups. D) The delta FC in the RSC mice was significant when compared to the delta FC of the CTRL mice (Mann-Whitney U test, FDR corrected; colors and labels as in panel (B). E) The strongest correlation decreases are plotted for the RSC, ACA, and Th groups.

5.2 Appendix B: SBI results from a different TVB parametrization

We use SBI to infer the configuration of local and global parameters ($\eta_{ACA}, \eta_{RSC}, \eta_{Th}, G$) that best explain the data features in the pre and post-silencing cases (see Methods). SBI predicts that focal region silencing induces local excitability changes and global network segregation, as measured by a decrease in the global coupling Supp.Fig.4.A, left. As expected, these changes were not significant in the CTRL group, as opposed to the RSC group. In particular, in Supp.Fig.4.A, right, we show that RSC, ACA, and Thalamus all have higher excitability after direct silencing, i.e., by local intervention. On the one hand, when the thalamus is lesioned, it is not predicted that the excitability of cortical hubs will change significantly. On the other hand, following either ACA or RSC silencing, the model infers decreased thalamic excitability η_{Th} and increased cortical excitabilities η_{ACA} and η_{RSC}. In other words, chemogenetic silencing is predicted to induce nonlocal changes in regions that are not directly silenced. The ACA and the RSC are strongly connected regions, as both are part of the DMN, and they show concurrent increases when either is shut down. The thalamus, on the contrary, is inferred to show decreased excitability after the chemogenetic silencing of these cortical hubs, which might be interpreted as a compensatory mechanism. To check for the robustness of our results, we have also used the model to infer the parameters that were best predictive of average features across subsets of mice (as opposed to fitting each mouse individually). As evident in Supp.Fig.4, we show that, as average features are evaluated over a growing number of mice, the results quickly converge to an even sharper distinction between the pre-and post-conditions (with the exception of the control group), in the same direction as those observed at the single-mouse level.

In conclusion, in this section, we have used probabilistic machine learning and mechanistic models to infer the most plausible local, microscopic mechanisms through which local lesions affect large-scale patterns of activities. We conclude that a decrease in network integration and an increase of excitability in the silenced regions, accompanied by nonlocal excitability changes, are possible candidates for causes of impairment.

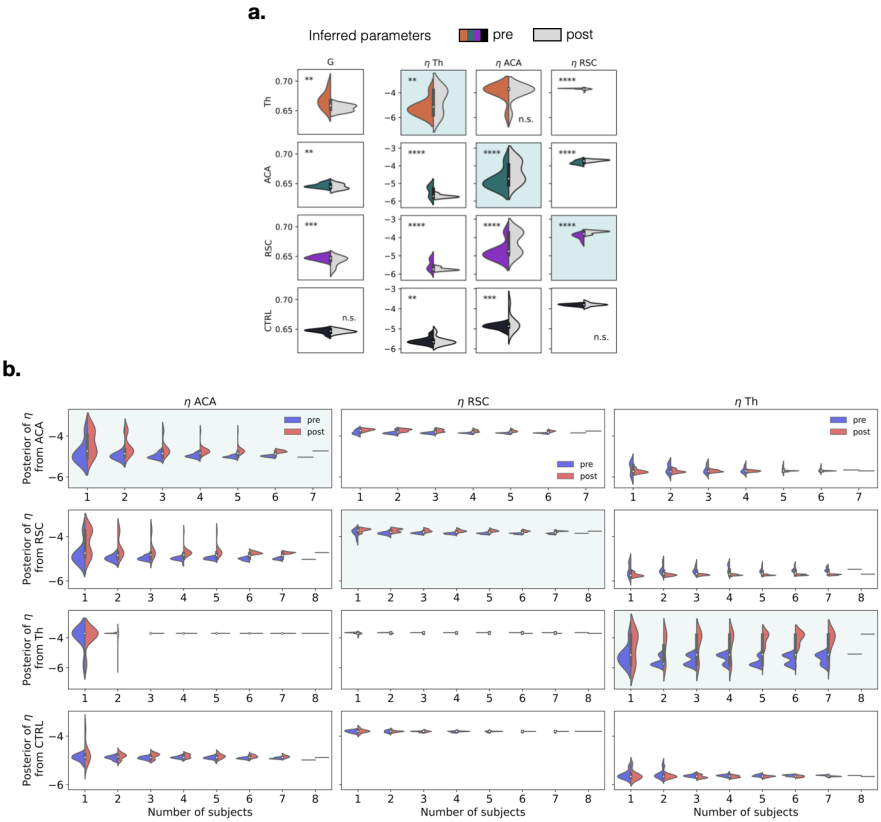

Fig. S5 SBI results from a different TVB parametrization (A) The estimated posterior distribution of the global coupling parameter G and the excitability parameter η in ACA, RSC, and Th groups, for pre-lesioning and post-lesioning ($p < 0.01$ (**), $p < 0.001$ (***), $p < 0.0001$ (****)), obtained by training a probabilistic deep learning algorithm, the so-called MAF (see Methods), on the summary statistics of simulations. Results indicate a significant increase in the corresponding regions by lesioning. (B) The estimated posterior distribution of the excitability parameter η in ACA, RSC, and Th groups, for pre-lesioning and post-lesioning. Here, the summary statistics are averaged over different subsets of mice.